Unmanned Aerial Vehicle Wireless Charging System With Orthogonal Magnetic Structure and Position Correction Aid Device

Shuai Wu, Chunwei Cai, *Member, IEEE*, Longyun Jiang, Jiawen Li, and Shiyan Yang

***Abstract*—Design and fabrication of a wireless charging system, which includes a wireless charging base station and an unmanned aerial vehicle (UAV) with wireless charging capability is proposed for enlarging the UAV's working range. First, an optimized magnetic coupler featuring with an orthogonal magnetic structure with a flexible soft magnetic core in receiver is proposed to ensure high efficiency and low-leakage magnetic flux interference. Second, a wireless charging circuit topology and a closed-loop power controller implemented on the primary side are designed and analyzed in detail to maintain constant current/constant voltage charging for the UAV. Then, a wireless charging station with position correction aid device is developed, which can achieve high-precision alignment. A prototype of the UAV wireless charging system with the proposed magnetic structure, primary-side control, and position correction are built and tested. Experimental results show that the fabricated wireless charging system can deliver 87.4 W at a dc-to-battery efficiency of 87.3%, and the system is adapted autonomous charging of UAV.**

***Index Terms*—Coil alignment, magnetic coupler, unmanned aerial vehicle (UAV), wireless charging.**

I. Introduction

THE usage and deployment of unmanned aerial vehicles (UAVs) is becoming increasingly prevalent. They are commonly used in inspection, delivery, search, and rescue, etc., [1]–[3]. Generally, UAVs are battery powered, the limited capacity of batteries cannot sustain sufficiently long cruising times. In the past, the UAVs must go back to a base station to charge, thus, the operation efficiency of UAVs is severely restricted and part of energy is wasted on the return trip rather than cruising route. Wireless charging is an enabling technology for UAVs since it can eliminate the manual intervention during charging. By setting relay charging stations in the cruise route of UAVs, the working range of UAVs can be effectively enlarged.

A major impediment to the adoption of wireless charging systems is the special structure and the limited payload of UAVs, which requires that the magnetic coupler has good adaptability to the UAV's structure and the weight of the pick-up system (which includes magnetic receiver and pick-up circuit) is as light as possible. Therefore, the design of the magnetic coupler and system circuit faces stringent requirements. Several different magnetic structures have been addressed in the literatures to achieve wireless charging for UAVs. The face-to-face circle or rectangle coil structures are most commonly used due to their simple geometry [4]–[13]. In [4] and [5], a nonpolarized transmitter and an air-cored receiving coil wrapped around the UAV's shield are adopted. Similarly, Song *et al.* [6] and Zhou *et al.* [7] placed the circle receiving coil under the body of the UAV. In the structures mentioned above, there will inevitably be a large air gap between transmitter and receiver, resulting in a low working efficiency and a poor EMC/EMI performance [8], [9]. In [10], a large rectangle receiving coil is installed at the bottom of landing gear legs. As the air gap is very small, the coupling ability is strong. But, the equipment under the UAV's body such as pan-and-tilt camera will also be exposed to strong magnetic field. To solve this problem, the magnetic cores or aluminum sheet are needed in the pick-up [11]–[13], but it will undoubtedly change the wind drag of the UAV and cause the flight instability. In [14], a small circle transmitting pad and a small circle receiving coil are adopted, and the receiving coil is placed on the bottom of one of the landing gears leg, so as to reduce wind drag and magnetic field operation range. However, due to the influence of assembly position, the receiving coil must be very small and the diameter of the used wire is limited, which results in that this magnetic structure is only suitable for the low-power charger. In [15], three dipole coils with ferrite are installed at the bottom of UAV's three landing gear legs, respectively, which requires changing the configuration of the original landing gears, and the magnetic coupler is easy to be impaired during landing due to brittle ferrite.

Manuscript received August 3, 2020; revised October 31, 2020; accepted December 19, 2020. Date of publication December 25, 2020; date of current version March 5, 2021. This work was supported in part by the Major Scientific and Technological Innovation Project in Shandong Province of China under Grant 2017CXGC0921 and in part by the Natural Science Foundation in Shandong Province of China under Grant ZR2019MEE052. Recommended for publication by Associate Editor R. Zane. *(Corresponding author: Chunwei Cai.)*

Shuai Wu is with the School of New Energy, Harbin Institute of Technology-Weihai, Weihai 264209, China, and also with the School of Electrical Engineering and Automation, Harbin Institute of Technology, Harbin 150001, China (e-mail: wushuai013@163.com).

Chunwei Cai and Longyun Jiang are with the School of New Energy, Harbin Institute of Technology-Weihai, Weihai 264209, China (e-mail: caichunwei@hit.edu.cn; wfjianglongyun@163.com).

Jiawen Li is with the Academy of Automation, Southeast University, Nanjing 210096, China (e-mail: theunknown0818@163.com).

Shiyan Yang is with the School of Electrical Engineering and Automation, Harbin Institute of Technology, Harbin 150001, China (e-mail: syyang@hit.edu.cn).

Color versions of one or more of the figures in this article are available online at https://doi.org/10.1109/TPEL.2020.3047384.

Digital Object Identifier 10.1109/TPEL.2020.3047384

To address those drawbacks, the authors proposed an orthogonal magnetic structure with a horizontal polarized transmitting pad and a vertical rectangle receiving coil for UAV wireless charging [16], [17]. This magnetic structure contributes to the better installation adaptability for UAVs special shape, lower weight of magnetic receiver, and larger power transfer capacity. In this article, the magnetic structure will be further improved by using Fe-based nanocrystalline flexible soft magnetic material in the receiver. The improved orthogonal magnetic structure allows the receiver to be lighter.

Another challenge with UAV wireless charging systems is the inevitable misalignment between the transmitter and receiver, which could significantly degrade the power transfer performance. The two following types of methods are suitable for coping with the misalignment problem. One of the types generate a magnetic field over a large range space by transmitter, such as enlarging the single transmitting coil dimension and adopting multiple coil arrays. In [4] and [9], the magnetic structures with a lager transmitting coil and a small receiving coil are presented for expanding the misalignment tolerance. Han *et al.* [18] develops a quasi-3D-omnidirectional UAV wireless charging system employing double 3-D transmitting coils. These solutions have the advantages of simple structure and low cost. However, the EMC/EMI performance is poor, which is extremely dangerous for the hardware of UAVs. To enlarge the effective charging area and also limit the operation space of the emission magnetic field, Campi *et al.* [19]–[21] developed a coil array transmitter for the UAV free-position-landing charging. A crucial link in multicoil array transmitter wireless charging system is to precisely detect the position of the receiver to decide the working transmitting coils. The current coil positioning methods actually rely on additional precision detecting hardware and complex detecting strategy [21]–[23], which would increase the complexity of the hardware and control system significantly and the likelihood of failure would be much higher in outdoor conditions. The other utilizes the extra alignment effort to achieve adaptive position correction. The coil alignment can be considered from aligning the transmitter to the receiver [24]–[27], and adjusting the vehicle for better alignment [28], [29]. To these is the premise of the coil position can be accurately sensed. Unfortunately, the accuracy of coil position sensing is unreliable in outdoor conditions at present. In this article, a new class of alignment technique is presented, where the coil-position detecting hardware is not needed and the UAV can be guided into a fixed location with fine accuracy.

In this article, a UAV wireless charging system with orthogonal magnetic structure and position correction aid device is developed. The proposed design is characterized by high efficiency, low EMC/EMI, economic and simple coil arrangement, effective configuration, and wider free landing area with the position correction. The rest of this article is organized as follows. The magnetic coupler design and analysis are presented in Section II. The wireless charging system circuit is developed in Section III. The details of the position correction are presented in IV. Section V is the experimental results of the prototype system. Finally, the conclusion is summarized in Section VI.

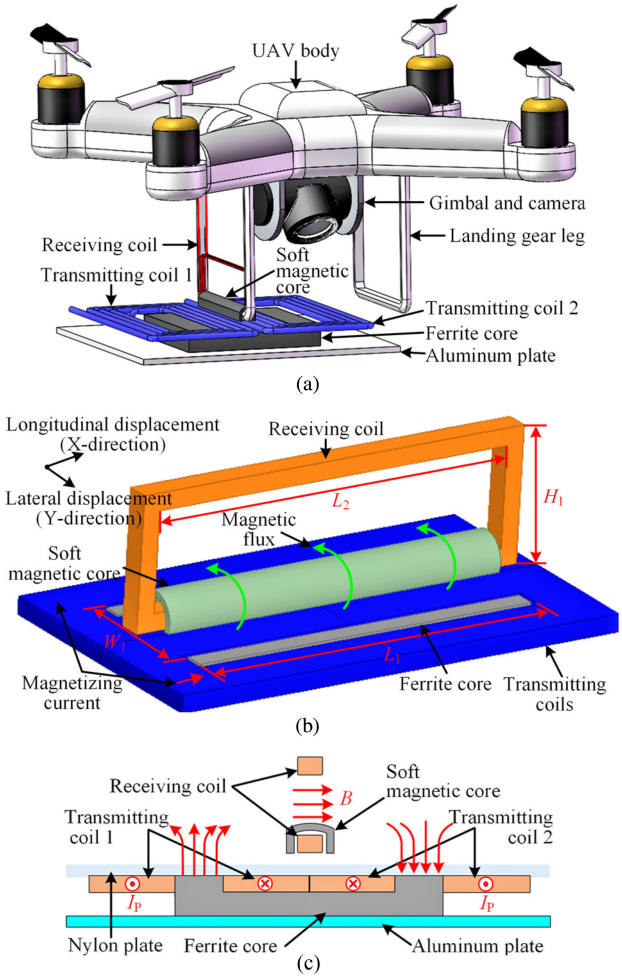

Fig. 1. (a) Overall configuration of the proposed UAV wireless charging system. (b) Proposed magnetic structure. (c) Flux distribution on a cross section.

II. Magnetic Coupler Design

A. Configuration of the Proposed Magnetic Coupler

The power system of the UAV wireless charging has two parts: one on the UAV body and the other one on the charging station. Accordingly, the magnetic coupler is divided into transmitter and receiver, and the proposed magnetic coupler is shown in Fig. 1. The transmitter consists of two rectangular coils, a flat-U type ferrite core and an aluminum backing plate. The two transmitting coils are respectively wound around the two side columns of the U-shaped ferrite core. The ferrite core plays an important role in lowering the magnetic resistance of the main magnetic circuit and guiding the majority of the flux out of the front of the transmitter. The current direction of each transmitting coil is reversed, leading to the reversed polarity of thrown magnetic flux B at each column of the ferrite core. Hence, the main magnetic flux circuit through the two columns of the ferrite core, and a horizontal flux is formed in the upper area in the middle of the core, as shown in Fig. 1(c), where I_P is the magnetizing current. The aluminum plate is used to reduce the flux leakage out of the back of the transmitter and add rigidity to the structure.

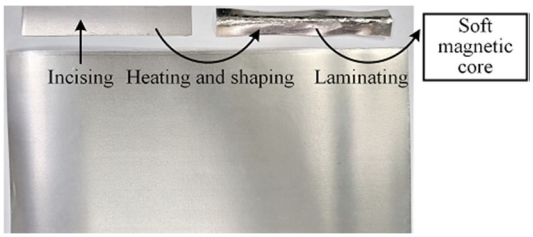

Fig. 2. Fe-based nanocrystalline flexible soft magnetic material.

TABLE I
COMPARISON OF THREE MAGNETIC MATERIALS

Parameters	Fe-based nanocrystalline ribbons	Ferrite PC40	Ferrite PC95
Manufacturers	CAETG	TDK	TDK
Saturation magnetic flux density (25 °C)	1250 mT	510 mT	530 mT
Initial permeability	1×10^4	0.23×10^4	0.33×10^4
Core loss (200 kHz, 200 mT)	550 kW/m^3	600 kW/m^3	350 kW/m^3
Physical property	Flexibility	Fragility	Fragility

The receiver consists of a rectangular coil and a flexible soft magnetic core. The receiving coil is placed vertically, which has two advantages. First, the landing gear is usually placed vertically, so the proposed magnetic structure is easy to embed the receiving coil into one of the landing gears, without changing the shape of the UAV, hence it has better adaptability on the UAV and it will not increase the wind resistance of UAV. Second, the receiving coil, placed vertically, can effectively pick up the horizontal flux thrown by the transmitter and realize the effective coupling between the transmitter and the receiver.

Adding magnetic cores is an effective way to improve the coupling performance and system efficiency. Although the ferrite is an optimized material for guiding the high-frequency magnetic flux in general wireless charging system, it might be less practical on the UAV's onboard side, since it is so fragile that it can be easily damaged during a UAV landing. In this article, a Fe-based nanocrystalline ribbons magnetic material is adopted in the receiver, as shown in Fig. 2, the parameters of this material are matched with those of the other two common ferrite materials as shown in TABLE I. It is shown that the performance of the Fe-based nanocrystalline ribbons is just slightly inferior to that of PC95 in terms of core loss. Meanwhile, the Fe-based nanocrystalline ribbons are more flexible, and it is better to adapt to the shape of a UAV. Through incising, heating and shaping, and multilayer laminating to form the desired shape of the flexible soft magnetic core, the structure of the flexible soft core used in this article is shown in Fig. 1(c), the receiving core is referred to as an inverted-U structure, which is wrapped only at the bottom of the receiving coil. The reason why the flexible soft magnetic core is only wrapped around the bottom edge of the receiving coil, but not placed on the top edge is that the magnetic resistance of the main magnetic circuit is reduced, and the magnetic resistance of the leakage magnetic circuit at the receiving side is not increased, so as to maximize the coupling.

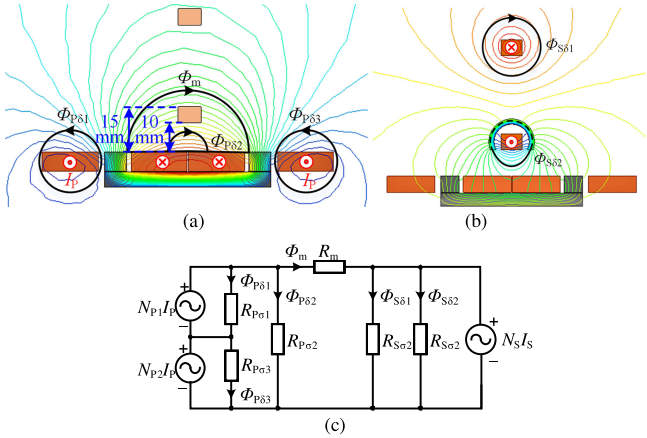

Fig. 3. (a) Distribution of magnetic flux lines thrown by the transmitter of a cross section when the receiving coil is not excited and no flexible soft core is added. (b) Distribution of magnetic flux lines thrown by receiver of a cross section when the transmitting coil is not excited and flexible soft core is added in the receiver. (c) Magnetic resistance circuit.

B. Dimensions Design of the Proposed Magnetic Coupler

It is important to deliver the maximum value of magnetic flux throw by transmitter to receiver, so as to improve the system coupling performance. As identified from Fig. 1(b), when the UAV type is determined, the landing gear size of the UAV will be determined accordingly. Since the receiving coil is nested on the landing gear leg, the length and maximum winding width of the receiving coil are also determined. In addition, the width of the transmitting coil is determined to the width of the transmitting core window. Therefore, only three major parameters, i.e., transmitting core window width W_1, transmitting core length L_1, and receiving coil height H_1 should be determined to complete the parameters design of the proposed magnetic coupler. As a position correction aid scheme is proposed in this article to ensure the accurate alignment of the magnetic coupler, the magnetic parameters design process does not need to consider misalignments. Therefore, the parameters design goal of this article is to improve the coupling capacity as much as possible and reduce the weight of the receiver.

The distribution of magnetic flux lines thrown by the transmitter and receiver is shown in Fig. 3(a) and (b), respectively, where Φ_{m} is main magnetic flux, $\Phi_{\mathrm{P}\delta1}$, $\Phi_{\mathrm{P}\delta2}$, $\Phi_{\mathrm{P}\delta3}$, $\Phi_{\mathrm{S}\delta1}$, and $\Phi_{\mathrm{S}\delta2}$ are leakage magnetic flux. The simplified magnetic circuit of the proposed magnetic structure can be derived further, as shown in Fig. 3(c). $N_{\mathrm{P}1}$ and $N_{\mathrm{P}2}$ are the turns of transmitting coil 1 and transmitting coil 2, $R_{\mathrm{P}\delta1}$, $R_{\mathrm{P}\delta2}$, $R_{\mathrm{P}\delta3}$, R_{m}, $R_{\mathrm{S}\delta1}$, and $R_{\mathrm{S}\delta2}$ are magnetic resistance of each magnetic flux branch mentioned above, neglecting all the magnetic resistance of ferrites. According to the simplified magnetic circuit and superposition theorem, the coupling coefficient can be calculated as

$$k = \frac{R_{\mathrm{m}}^2}{R_{\mathrm{P}\sigma}R_{\mathrm{S}\sigma} + R_{\mathrm{P}\sigma}R_{\mathrm{m}} + R_{\mathrm{S}\sigma}R_{\mathrm{m}} + R_{\mathrm{m}}^2} \tag{1}$$

where $R_{\mathrm{P}\delta}$ and $R_{\mathrm{S}\delta}$ are the total primary leakage reluctance and total secondary leakage reluctance, respectively, which can be

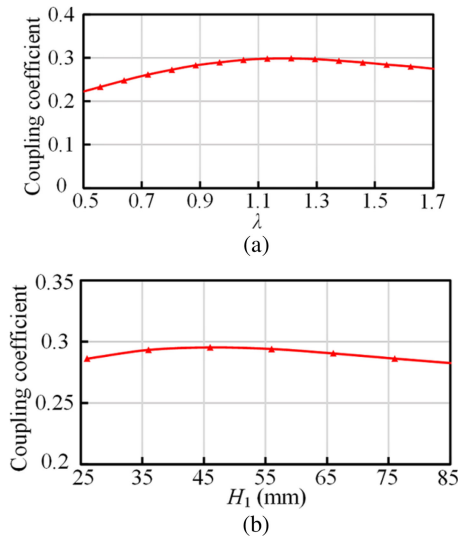

Fig. 4. (a) Simulation results of coupling coefficient k for various λ. (b) Simulation results of coupling coefficient k for various H_1 when $W_1 = 35$ mm.

expressed by (2) when N_{P1} is equivalent with N_{P2}

$$R_{\mathrm{P}\sigma} = (R_{\mathrm{P}\sigma 1} + R_{\mathrm{P}\sigma 3})||R_{\mathrm{P}\sigma 2},$$
$$R_{\mathrm{S}\sigma} = R_{\mathrm{S}\sigma 1}||R_{\mathrm{S}\sigma 2}. \tag{2}$$

Any kth magnetic resistance R_{k} mentioned above can be calculated by (3), $\mu_0 = 4\pi \times 10^{-7}$ H/m, l_{k} is length of a magnetic path, and $A_{\mathrm{eff,k}}$ is an effective area [30]

$$R_{\mathrm{k}} = \frac{l_{\mathrm{k}}}{\mu_0 A_{\mathrm{eff},k}}. \tag{3}$$

Since l_{k} and $A_{\mathrm{eff,k}}$ of the proposed magnetic coupler cannot be easily calculated, it is difficult to determine R_{k} by hands. Therefore, a finite element analysis method based on the ANSYS Maxwell simulation is adopted for finding the optimum value of the variables for maximum coupling coefficient k.

Define variable λ, which is equal to L_2 (length of the receiving coil) over L_1. As shown in Fig. 4(a), k becomes lager when λ increases, because as L_2 increases, more and more thrown horizontal magnetic flux passes through the receiving coil. Note that k no longer increases if λ is much bigger than 1, because the horizontal flux that can be captured by the receiving coil has reached the maximum value. If L_2 continues to increase, the leakage flux of the receiving coil will increase. Based on this, L_1 is set at 130 mm, which is equal to L_2.

The main magnetic flux path height is roughly proportional to one half of W_1, as shown in Fig. 3(a). Restricted by the landing gear of the UAV, the distance between the upper edge of the receiving coil and the plane of the transmitting coil is 15 mm. Therefore, in order to ensure the effective coupling between the transmitter and the receiver, W_1 needs to be greater than or equal to 30 mm. Meanwhile, if W_1 is too large, it will lead to a large magnetic field operation space, resulting in a large magnetic leakage of the system. Based on this, W_1 is set to 35 mm.

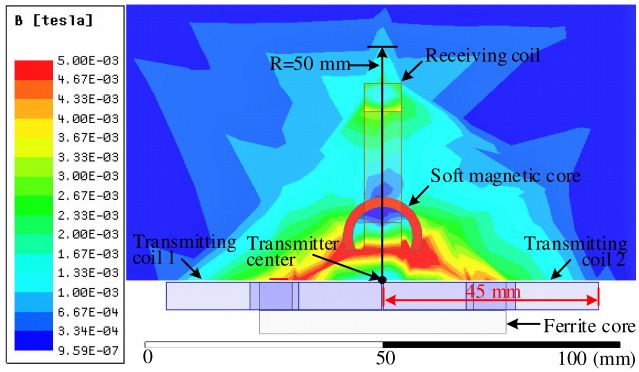

Fig. 5. Magnetic field distribution in the cross-section, the range of the magnetic flux is 0.96-5 $\times$ 10^3 μT. (The applied transmitter and receiver peak currents for simulation are 5 and 8.5 A).

When W_1 is equal to 35 mm and H_1 is changed, various k are shown in the Fig. 4(b). The k increases first and then decreases with the increasing of H_1. Because the height of thrown magnetic flux is limited, if the receiving coil is set too high, the leakage inductance of the receiver will be increased, but the effective magnetic flux receiving area will not be increased. As H_1 continues to decrease, more and more thrown magnetic flux will not be picked up by the receiving coil, and more and more leakage magnetic flux by receiver will flow through the flexible soft magnetic core, which will also reduce the magnetic resistance of the leakage magnetic circuit. As shown in Fig. 4(b), when H_1 is between 35 and 55 mm, the coupling coefficient is large. In order to reduce the weight of the receiver as much as possible, H_1 is set as 35 mm.

C. Magnetic Distribution of the Proposed Magnetic Coupler

The magnetic structure and parameters are settled by the above procedure. Then, the magnetic field behavior of the proposed magnetic structure is further studied, and the magnetic distribution is shown in Fig. 5. The bipolar transmitter has an obvious effect to constraint the leakage magnetic field, and the soft magnetic core in receiver further guides the magnetic flux, which obviously restricts the operation range of the magnetic field. It can be seen from Fig. 5 that the main operation space of the magnetic field is within a semicircle 50 mm away from the center of the transmitter, and the magnetic field will rapidly decay outside the semicircle. In addition, the receiver is installed at the bottom of the UAV landing gear to keep the magnetic field away from the UAV body. Based on the above analysis, it can be found that the magnetic field operation space of the proposed magnetic coupler is small, and the magnetic field operation space is far away from the UAV body, which guarantees the safety of UAV onboard equipment.

III. System Circuit and Primary Control Design of the Wireless Charging System

A. System Circuit Structure Design

The developed power system circuit is shown in Fig. 6(a). The subsystem of the charging station consists of a dc voltage

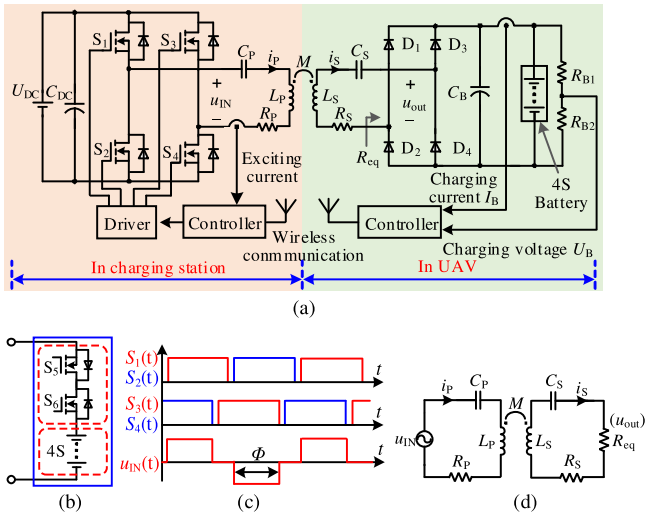

Fig. 6. (a) Power system circuit configuration. (b) 4S battery pack. (c) Gate drive signals and output voltage of inverter. (d) Equivalent circuit model.

source (U_{DC}), a H-bridge inverter (switch by S_1–S_4), a magnetic transmitter (self-inductance L_P and parasitic resistance R_P), and a series compensation capacitor (C_P). The inverter converts the dc-source to an 85 kHz ac waveform. The inverter is controlled by the phase shift modulation scheme, and its gate drive signals and output voltage are shown in Fig. 6(c), where Φ is conduction angle, u_{IN} and i_P are its output voltage and current, respectively. Then, the transmitter is excited to produce magnetic field. The other subsystem on the UAV body, where a magnetic receiver (self-inductance L_S and parasitic resistance R_S), a series compensation capacitor (C_S), a H-bridge rectifier (diodes D_1-D_4), and a battery pack are included. The receiver is coupled to the transmitter by mutual inductance M. Then, the picked ac power flows through the compensation circuit, rectifier, and filter to charge the battery. The characteristic of the wireless charging system depends on the compensation topologies for resonance in series, parallel, LCL, or LCC [31]–[33]. In this design, the series–series (SS) compensation is adopted since its output behaves constant current, which is a natural advantage for lithium-battery charging. A current sensor and a voltage sensor are used in the output of the system to measure the charging current I_B and charging voltage U_B. Moreover, a wireless communication network that feeds I_B and U_B back to the controller of the charging station is made to maintain the constant current (CC)/ constant voltage (CV) charging for UAV's battery.

System safety should be an important aspect for the UAV wireless charging system, which includes two aspects: battery safety and charging system safety. Without considering series battery's charge balanced control, three countermeasures are developed to improve the system security in this article.

1) Connect two switches of MOSFET in series with the battery, shown in Fig. 6(b), which can be used to disconnect the battery from the charging system in case of emergency to protect the battery.
2) According to the following analysis, SS compensation is not allowed to operate at no-load state, otherwise the excitation current will surge. A current detection system, as shown in Fig. 6(a), is placed at the primary side to monitor the excitation current to ensure system safety.
3) Miscommunication is also a risk of power system. In this design, only if the primary controller gets the correct feedback from the pick-up will the primary controller output PWM to inverter. Otherwise, the system stops charging and restarts the wireless communication.

B. Steady-State Analysis of the Developed Topology

In order to determine the steady-state characteristics of the system, the fundamental mode analysis is adopted, which is effective in the analysis of resonance network. As shown in Fig. 6(c), the voltage rms U_{IN} of u_{IN} (fundamental output voltage of the inverter) is obtained by Fourier decomposition method as

$$U_{IN} = \frac{2\sqrt{2}}{\pi} U_{DC} \sin\left(\frac{\phi}{2}\right). \tag{4}$$

The series compensation is used at the receiving side, leading to a sine input current ware of the rectifier. Then, a capacitor filter is used to smooth the output charging current I_B, which can be derived as

$$I_B = \frac{1}{2\pi}\int_0^{2\pi} \left|\sqrt{2} I_S \sin(\omega t)\right| \mathrm{d}wt = \frac{2\sqrt{2} I_S}{\pi} \tag{5}$$

where ω is the operation angular frequency of the system.

Neglecting the power losses of the rectifier and filter, the output charging voltage can be obtained as

$$U_B I_B = U_{out} I_S \Rightarrow U_B = \frac{\sqrt{2}\pi U_{out}}{4} \tag{6}$$

where U_{out} is rms of the SS compensation network output voltage u_{out} and I_S is rms of i_S.

According to KVL, Fig. 6(d) can be described by

$$\begin{cases} (j\omega L_P + 1/j\omega C_P + R_P) I_P - j\omega M I_S = U_{IN} \\ (j\omega L_S + 1/j\omega C_S + R_P + R_{eq}) I_S - j\omega M I_P = 0 \end{cases} \tag{7}$$

where I_P is rms of i_P.

In order to ensure that the system has large transmission capacity and high efficiency, the compensation network is designed to work in resonant state, and SS compensators' parameters should be satisfied the following equation:

$$\omega = \frac{1}{\sqrt{L_P C_P}} = \frac{1}{\sqrt{L_S C_S}}. \tag{8}$$

Substituting (3) and (5) into (2) results in I_B as

$$I_B = \frac{8}{\omega M \pi^2} \sin\left(\frac{\phi}{2}\right) U_{DC}. \tag{9}$$

Then, U_B can be further expressed by

$$U_B = \frac{8}{\omega M \pi^2} \sin\left(\frac{\phi}{2}\right) U_{DC} R_B \tag{10}$$

where R_B is equivalent load resistance of the charging battery, which is defined as the ratio of U_B to I_B [34]. According to (9) and (10), it is obvious that the charging voltage or current can be adjusted by controlling the conduction angle of the inverter.

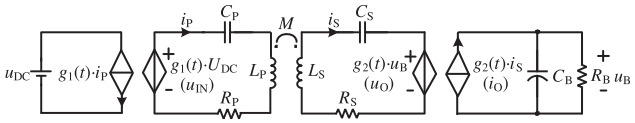

Fig. 7. Equivalent circuit model of the designed wireless charging system.

C. Small-Signal Modeling and Practical Primary Controller Implementation

To practically realize the charging power regulation and reduce the on-board receiving subsystem weight as much as possible, primary side control based inverter is implemented. The conduction angle Φ of the inverter's driving PWM signal is used as the control variable to maintain the CC/CV charging. In order to design the practical primary controller, the small signal model of the system is deduced.

According to the open-loop structure of Fig. 6(a), an equivalent circuit model can be established in Fig. 7, which simplifies the nonlinear links in the circuit and will be applied to the generalized state space averaging (GSSA) method. Considering the case where the conduction angle is Φ and selecting the output voltage of inverter as the zero-phase reference, the influence of dead time of the PWM signal is ignored. Then, the commutation functions $g_{1(t)}$ and $g_{2(t)}$ are defined in the following equation:

$$g_1(t)=\begin{cases}1 & t\in[\frac{t_0}{2},\frac{T-t_0}{2}]\\ -1 & t\in[\frac{T+t_0}{2},T-\frac{t_0}{2}]\end{cases}$$
$$g_2(t)=\begin{cases}1 & t\in[-\frac{\varphi}{2\pi}T,(-\frac{\varphi}{2\pi}+\frac{1}{2})T]\\ -1 & t\in[(-\frac{\varphi}{2\pi}+\frac{1}{2})T,(-\frac{\varphi}{2\pi}+1)T]\end{cases} \tag{11}$$

where T is the period of the PWM signal and t_o is equal to $(\pi - \Phi)/\omega$, φ is the $g_2(t)$'s phase leads of $g_1(t)$. Then, differential equations can be written as

$$\begin{cases}L_P\frac{di_P}{dt}=u_{IN}-i_PR_P-u_{CP}+M\frac{di_S}{dt}\\ C_P\frac{du_{CP}}{dt}=i_P\\ L_S\frac{di_S}{dt}=-u_O-i_SR_S-u_{CS}+M\frac{di_P}{dt}\\ C_S\frac{du_{CS}}{dt}=i_S\\ C_B\frac{du_B}{dt}=i_O-\frac{u_B}{R_B}.\end{cases} \tag{12}$$

The inductor current and capacitor voltage can be expressed as follows:

$$\begin{cases}\langle i_P\rangle_1=x_1+jx_2\\ \langle u_{CP}\rangle_1=x_3+jx_4\\ \langle i_S\rangle_1=x_5+jx_6\\ \langle u_{CS}\rangle_1=x_7+jx_8\\ \langle u_B\rangle_0=x_9\end{cases}\Rightarrow\begin{cases}i_P=2x_1\cos\omega t-2x_2\sin\omega t\\ u_{CP}=2x_3\cos\omega t-2x_4\sin\omega t\\ i_S=2x_5\cos\omega t-2x_6\sin\omega t\\ u_{CS}=2x_7\cos\omega t-2x_8\sin\omega t\\ u_B=x_9\end{cases} \tag{13}$$

where $x_1 - x_9$ are state variables of the GSSA model, $\langle i_P\rangle_1$, $\langle u_{CP}\rangle_1$, $\langle i_S\rangle_1$, and $\langle u_{CS}\rangle_1$ are the first-order Fourier coefficients of ac signals, and $\langle u_B\rangle_0$ is the zero-order Fourier coefficient of dc output charging voltage.

Further, according to the definition of Fourier series, the expressions of $\langle g_1(t)\rangle_1$ and $\langle g_2(t)\rangle_2$ can be obtained as

$$\begin{aligned}\langle g_1(t)\rangle_1&=\frac{1}{T}\int_{\frac{t_0}{2}}^{\frac{T-t_0}{2}}e^{-j\omega t}dt+\frac{1}{T}\int_{\frac{T+t_0}{2}}^{T-\frac{t_0}{2}}-e^{-j\omega t}dt\\ &=-\frac{2j}{\pi}\sin\left(\frac{\phi}{2}\right)\end{aligned} \tag{14}$$

$$\begin{aligned}\langle g_2(t)\rangle_1&=\frac{1}{T}\int_{-t_1}^{\frac{T}{2}-t_1}e^{-j\omega t}dt+\frac{1}{T}\int_{\frac{T}{2}-t_1}^{T-t_1}-e^{-j\omega t}dt\\ &=\frac{2}{\pi}(\sin\varphi-jcos\varphi)\end{aligned} \tag{15}$$

where $t_0=(\pi-\Phi)/\omega$ and $t_1=\varphi/\omega$, and $<g_1(t)>_1$, $<g_2(t)>_1$ are the first-order Fourier coefficients of $g_1(t)$, $g_2(t)$, respectively.

According to (14), (15) and the convolution of Fourier coefficients, the voltage and current of the nonlinear elements mentioned in (12) can be written as

$$\begin{aligned}u_{IN}&=\langle g_1(t)u_{DC}\rangle_1=\langle g_1(t)\rangle_1\langle u_{DC}\rangle_0+\langle g_1(t)\rangle_{-1}\langle u_{DC}\rangle_0\\ &=\frac{4}{\pi}u_{DC}\sin\left(\frac{\phi}{2}\right)\sin(\omega t)\end{aligned} \tag{16}$$

$$\begin{aligned}u_O&=\langle g_2(t)u_B\rangle_1=\langle g_2(t)\rangle_1\langle u_B\rangle_0+\langle g_2(t)\rangle_{-1}\langle u_B\rangle_0\\ &=\frac{4}{\pi}u_B[\sin(\omega t)\cos(\varphi)+\cos(\omega t)\sin(\varphi)]\end{aligned} \tag{17}$$

$$\begin{aligned}i_O&=\langle g_2(t)i_S\rangle_0=\langle g_2(t)\rangle_{-1}\langle i_S\rangle_1+\langle g_2(t)\rangle_1\langle i_S\rangle_{-1}\\ &=\frac{4\sin(\varphi)}{\pi}x_5-\frac{4cos(\varphi)}{\pi}x_6\end{aligned} \tag{18}$$

where $\langle g_1(t)\rangle_{-1}$, $\langle g_2(t)\rangle_{-1}$, and $\langle i_S\rangle_{-1}$ satisfy the conjugate relationship with $\langle g_1(t)\rangle_1$, $\langle g_2(t)\rangle_1$, and $\langle i_S\rangle_1$, respectively.

Through the parameter preparation from (13) to (18), the differential equations of the state variables can be derived as (19), shown at bottom of next page, where Δ is $L_PL_S - M^2$. In order to get the small signal model of the system, the state space expression needs to be first obtained as

$$\begin{cases}\dot{X}=AX+BU\\ Y=CX\end{cases} \tag{20}$$

where A, B, and C are input matrix of (17), they are given by (21), shown at bottom of next page. The state variables X, input vector U, and output vector Y are expressed by $X=[x_1, x_2 \ldots, x_9]^T$, $U=u_{DC}\sin(\Phi/2)$, and $Y=u_B$

After eliminating the steady-state components, the small signal transfer function can be described by

$$G_1(s)=\frac{\hat{y}(s)}{\hat{u}(s)}=\mathbf{C}(s\mathbf{I}-A)^{-1}\mathbf{B} \tag{22}$$

where I is the identity matrix which has the same number of rows and columns with matrix A. Substituting the relevant circuit parameters, listed in Table II, into (21) and (22), an open-loop transfer function can be obtained. As is shown in Fig. 8, the GSSA model can well reflect the transient and steady-state characteristics of the system. The developed GSSA model can be used for the controller design.

TABLE II
PARAMETERS OF WIRELESS CHARGING SYSTEM

Parameters	Value	Parameters	Value
U_{DC}	40 V	k	0.287
L_P	62.18 μH	L_S	16.47 μH
R_P	101.92 mΩ	R_S	76.71 mΩ
C_P	56.2 nF	C_S	213 nF
f	85 kHz	Weight of receiver	56.4 g

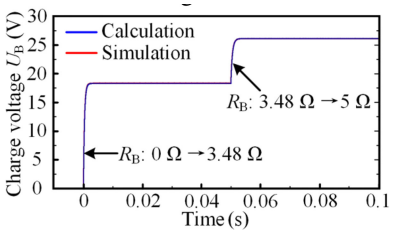

Fig. 8. Comparison of the step response of the GSSA model and simulation system.

The designed closed-loop control diagram for CC/CV charging is shown in Fig. 9(a), it consists of an outer voltage loop and an inner current loop. At the beginning of charging, U_B is small leading to a large voltage error e_u, which will cause the voltage PI controller to saturate, and then the current loop will complete the CC control. When U_B exceeds reference voltage V_{ref}, a negative error will be generated, which makes the voltage PI controller desaturated. In this stage, the current error e_i is always close to 0, and the current loop hardly works, while the voltage

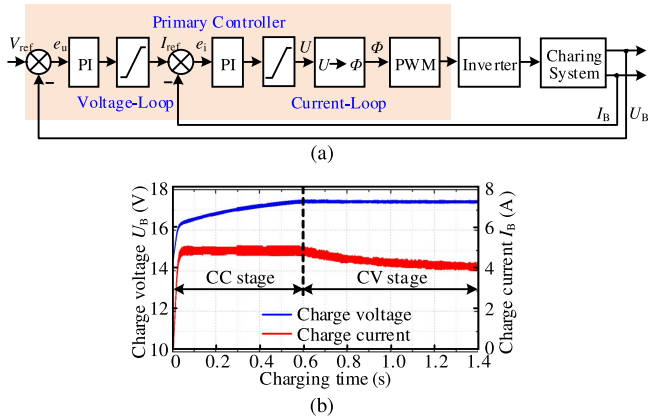

Fig. 9. (a) Workflow of the wireless charging system. (b) Charging voltage and charging current.

PI controller maintains the stability of charging voltage. Then, combined with the designed control system shown in Fig. 9(a), the charging current I_B and charging voltage U_B versus time are also obtained, as shown in Fig. 9(b), it can be found that the designed control system can realize the CC/CV charging task.

IV. WIRELESS CHARGING STATION CONFIGURATION AND OPERATION PRINCIPLE

A. Overall Configuration of the Station System

Fig. 10 illustrates the structure of the developed UAV wireless charging station, which is only for principal explanation, not

$$\begin{cases}
\frac{dx_1}{dt} = -\frac{L_S R_P}{\Delta}x_1 + \omega x_2 - \frac{L_S}{\Delta}x_3 - \frac{MR_S}{\Delta}x_5 - \frac{M}{\Delta}x_7 - \frac{2M\sin\varphi}{\pi\Delta}x_9 \\
\frac{dx_2}{dt} = -\omega x_1 - \frac{L_S R_P}{\Delta}x_2 - \frac{L_S}{\Delta}x_4 - \frac{MR_S}{\Delta}x_6 - \frac{M}{\Delta}x_8 + \frac{2M\cos\varphi}{\pi\Delta}x_9 - \frac{L_S}{2\Delta}u_{IN} \\
\frac{dx_3}{dt} = \frac{1}{C_P}x_1 + \omega x_4 \\
\frac{dx_4}{dt} = \frac{1}{C_P}x_2 - \omega x_3 \\
\frac{dx_5}{dt} = -\frac{MR_P}{\Delta}x_1 - \frac{M}{\Delta}x_3 - \frac{L_P R_S}{\Delta}x_5 + \omega x_6 - \frac{L_P}{\Delta}x_7 - \frac{2L_P\sin\varphi}{\pi\Delta}x_9 \\
\frac{dx_6}{dt} = -\frac{MR_P}{\Delta}x_2 - \frac{M}{\Delta}x_4 - \omega x_5 - \frac{L_P R_S}{\Delta}x_6 - \frac{L_P}{\Delta}x_8 + \frac{2L_P\cos\varphi}{\pi\Delta}x_9 - \frac{M}{2\Delta}u_{IN} \\
\frac{dx_7}{dt} = \frac{1}{C_S}x_5 + \omega x_8 \\
\frac{dx_8}{dt} = \frac{1}{C_S}x_6 - \omega x_7 \\
\frac{dx_9}{dt} = \frac{4}{\pi C_B}(x_5\sin\varphi - x_6\cos\varphi) - \frac{1}{C_B R_B}x_9
\end{cases} \tag{19}$$

$$A = \begin{bmatrix}
-\frac{L_S R_P}{\Delta} & \omega_0 & -\frac{L_S}{\Delta} & 0 & -\frac{MR_S}{\Delta} & 0 & -\frac{M}{\Delta} & 0 & -\frac{2M\sin\varphi}{\pi\Delta} \\
-\omega_0 & -\frac{L_S R_P}{\Delta} & 0 & -\frac{L_S}{\Delta} & 0 & -\frac{MR_S}{\Delta} & 0 & -\frac{M}{\Delta} & \frac{2M\cos\varphi}{\pi\Delta} \\
\frac{1}{C_P} & 0 & 0 & \omega_0 & 0 & 0 & 0 & 0 & 0 \\
0 & \frac{1}{C_p} & -\omega_0 & 0 & 0 & 0 & 0 & 0 & 0 \\
-\frac{MR_P}{\Delta} & 0 & -\frac{M}{\Delta} & 0 & -\frac{L_P R_S}{\Delta} & \omega_0 & -\frac{L_p}{\Delta} & 0 & -\frac{2L_P\sin\varphi}{\pi\Delta} \\
0 & -\frac{MR_P}{\Delta} & 0 & -\frac{M}{\Delta} & -\omega_0 & -\frac{L_P R_S}{\Delta} & 0 & -\frac{L_P}{\Delta} & \frac{2L_P\cos\varphi}{\pi\Delta} \\
0 & 0 & 0 & 0 & \frac{1}{C_s} & 0 & 0 & \omega_0 & 0 \\
0 & 0 & 0 & 0 & 0 & \frac{1}{C_s} & -\omega_0 & 0 & 0 \\
0 & 0 & 0 & 0 & \frac{4\sin\varphi}{\pi C_B} & -\frac{4\cos\varphi}{\pi C_B} & 0 & 0 & -\frac{1}{C_B R_B}
\end{bmatrix}$$

$$B = \left[0, \frac{-2L_S}{\pi\Delta}, 0, 0, 0, \frac{-2M}{\pi\Delta}, 0, 0, 0\right]^T, C = [0,0,0,0,0,0,0,0,1] \tag{21}$$

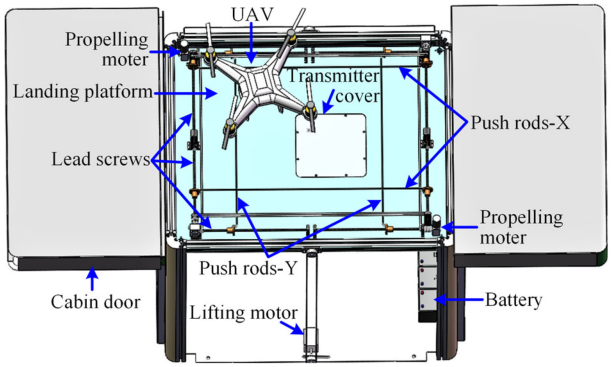

Fig. 10. Developed UAV wireless charging station.

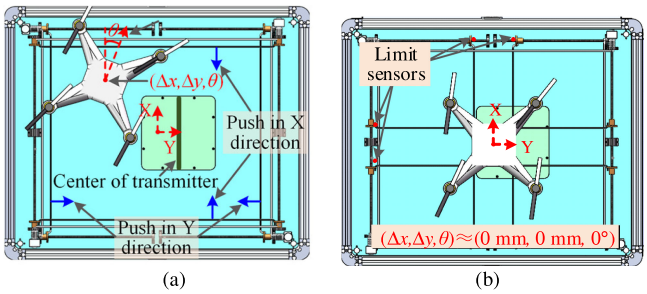

Fig. 11. Top view of the proposed wireless charging station. (a) Original location and (b) state after self-alignment.

for actual scale drawing. The charging station consists of the following three sections: 1) energy system; 2) station system; and 3) wireless charging system. In energy system, solar power generation and energy storage system are included to provide the energy needed for charging station operation and UAV charging. As for station system, it includes three functional modules: hatch-door opening and closing control, landing platform lifting control, and position correction control. The function of landing platform lifting control is to ensure the safety of UAV landing. For wireless charging system, the transmitter is mounted on the landing platform. After the UAV landing and position correcting, the transmitter is excited and the UAV is charged wirelessly.

B. Position Correction System

Due to the influence of detection accuracy, UAV control accuracy, UAV landing rebound and external force, it is difficult for UAV to achieve centimeter-level landing accuracy in the wilderness environment. Although the method of expanding the range of magnetic field operation by optimizing the magnetic design can cope with misalignment problem, it will reduce the overall efficiency and EMC/EMI performance of the system. Therefore, an additional position correction aid mechanical for the magnetic coupler is developed in this charging station, which is shown in Fig. 11. The position correction aid mechanical mainly consists of three parts:

1) four push rods, which can be divided into two groups performing longitudinal (*X*-direction) and lateral (*Y*-direction) position correction, respectively;
2) four or eight lead screws, which rotate and use the screw nut to drive the push rod movement;
3) one or two propelling motors, which are used to drive the screw rods.

The landing position of a UAV is random on the landing platform, as shown in Fig. 11(a), there are significant longitudinal misalignment Δx, lateral Δy, and rotational misalignment θ. Start the position correction aid device, with the push rods forward, the Δx, Δy, and θ gradually reduce. When the UAV is pushed to the center position of the landing platform, the magnetic coupler is precisely aligned, as shown in Fig. 11(b). The push and return distance of the push rods can be accurately controlled by stepper motors and positive stop limit-sensors, so the proposed scheme has the advantages of high precision and high reliability. In addition, there is no need to accurately detect the landing position of UAV and judge whether the coil is accurately aligned, the designed position correction aid system has the advantages of simple structure and reliable performance. It should be mentioned that the position correction aid device will be powerless when the UAV landing angle θ is greater than or equal to 45°. The UAV and the charging base station need to communicate in advance to determine the landing direction, and use the compass equipped by the UAV to roughly land in the specified direction.

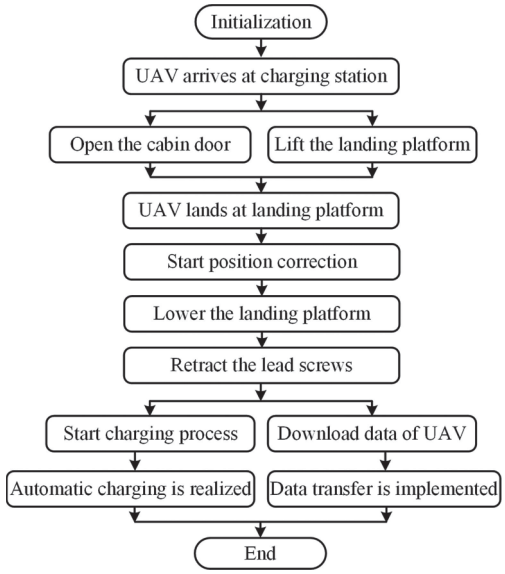

Fig. 12. Workflow of the UAV wireless charging system.

C. Operation Principle of the Station System

The workflow of the charging station system is plotted in Fig. 12, and the operating principles are as follows.

1) When a UAV arrives at the charging station, the cabin door of the charging station is opened and the landing platform is lifted.
2) After the UAV's landing is completed, the position correction aid mechanical is started. Until the position correction is completed, the landing platform is lowered to the initial position, and the cabin door is closed.

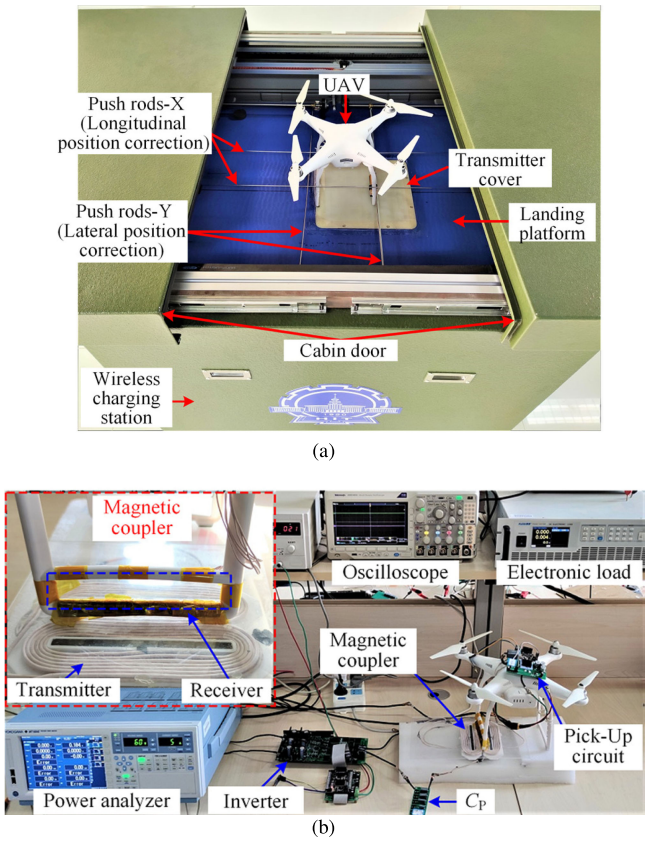

Fig. 13. Experiment setup of the UAV wireless charging system. (a) Wireless charging station. (b) Wireless charging system test platform.

3) Retract the lead screws of the position correction aid mechanical to the initial position, and then start charging process and download the UAV's data.
4) After the charging process is completed and the UAV receives the next flight order, the cabin door is opened and the UAV takes OFF.

V. System Manufacture and Validation

A. Experimental Prototype Manufacture

To demonstrate the proposal, an experimental prototype and a wireless charging system test platform with the parameters in Table II is constructed, as shown in Fig. 13. The system operates at 85 kHz with a fixed frequency. SiC MOSFETs C2M0080120D are used in the primary inverter, Schottky diodes DST1045S are used in the secondary rectifier. The charging voltage and charging current are sample by the secondary controller, and then this information is feedback to primary controller through the 2.4-GHz wireless communication modules. The coils in the transmitter are made of Litz wire of 0.1 mm $\times$ 400 strands, and the coil in the receiver is made of Litz wire of 0.07 mm $\times$ 300 strands. In addition, the PC40 from TDK ferrite core and aluminium sheet are adopted in the transmitter, and Fe-based nanocrystalline flexible soft magnetic core is used in the receiver, as mentioned in Section II. The weight of the magnetic receiver is 56.4 g, which has little impact on a UAV.

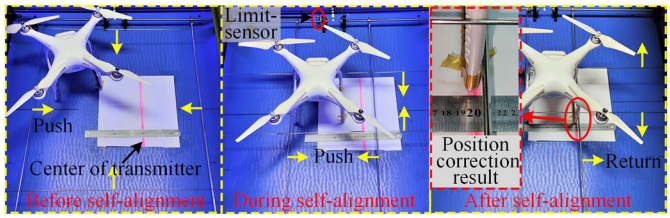

Fig. 14. Experiment of UAV position self-alignment.

As shown in Fig. 14, multiple tests verify that the magnetic coupler can be precisely aligned with the designed position correction aid scheme, and the lateral and longitudinal misalignment range after position correcting is always less than 5 mm. Therefore, the positioning scheme in this article has the advantages of high precision and high reliability.

B. System Performance Test Using Resistive Loads

Fig. 13(b) shows the wireless charging system view for a rated power test. The output of the system is linked to an electronic resistive load, which is used to simulate the load of a charging battery. Fixed load is set as 3.48 Ω, the output charging current in CC charging stage is set to 5 A, and the charging voltage in CV charging stage is set to 17.4 V. At the turning point of CC stage to CV stage, the maximum power of the system is 87 W. Of course, the designed system supports higher power transmission, because the magnetic flux density is far from the saturation value of the magnetic core. The result of the rated power test is shown in Fig. 15. The output voltage and output current of the inverter are almost in phase with each other, as shown in Fig. 15(a), so the inverter has only a real load leading to a high working efficiency of the inverter.

The input and output power are tested by Yokogawa WT1804E Power Analyzer at the rated power load, as shown in Fig. 15(b). Its input power is 100.1 W, output charging power is 87.4 W, and the whole system efficiency is 87.3%. Meanwhile, the charging current is 5 A, and charging voltage is 17.4 V, which meets the design requirements of the system. The system losses at the rated power load are further analyzed, as shown in Fig. 15(c). The losses mainly consist of three parts: inverter loss, magnetic coupler loss, and rectifier loss, and the efficiency of each part is 94.97%, 94.32%, and 97.22%, respectively. Due to the large capacity of the inverter used in this experiment, the inverter efficiency can be further improved by using the small capacity inverter.

With the designed control scheme, the charging voltage, charging current, charging power, and system efficiency of the closed-loop wireless charging system versus load resistance are plotted in Figs. 16 and 17. With the linear increase of load resistance, the conduction angle Φ of the inverter is automatically adjusted by the PID controller. Therefore, during the complete process, the 5 A constant charging current and 17.4 V constant charging voltage are achieved. Meanwhile, the whole system efficiency maintains above 86% in the high-power charging stage with load resistance of 3–5 Ω (the output charging power

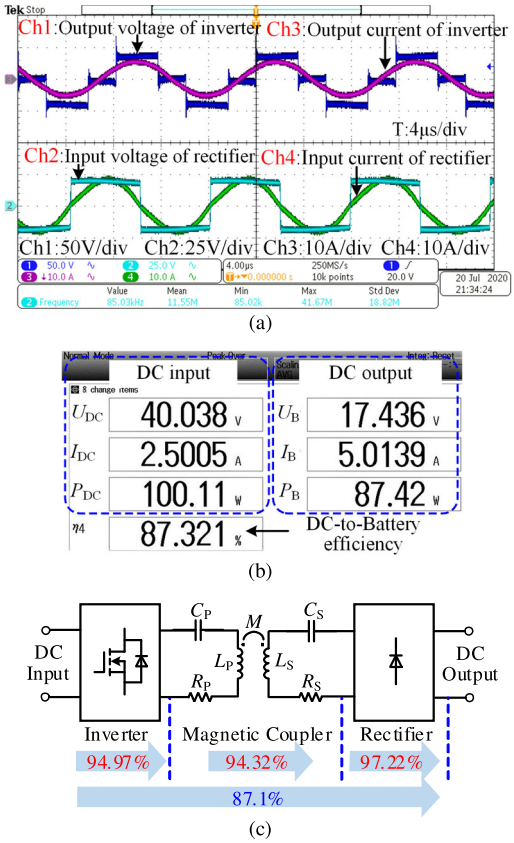

Fig. 15. Rated power test for the 3.48 Ω fixed resistive load. (a) System working waveforms. (b) DC-input and charging output power. (c) System losses analysis.

is greater than 78 W, and most of the charging time is spent in this stage).

Fig. 18 shows the variations of the output power and system efficiency against lateral and longitudinal misalignment in the open-loop condition. The coil positioning errors are less than or equal to 5 mm in this article. It is shown that both the output power and system efficiency are very stable in this misalignment range. With further increase of the misalignment, the output power is lifted, but this is at the cost of the sharp increase of the output current of the inverter, which leads to the decrease of the system efficiency. Therefore, an auxiliary alignment equipment for accurate alignment of the magnetic coupler in the wireless charging station is necessary for achieving high efficiency.

C. Application to the UAV

This experiment is conducted by applying the developed wireless charging system to the actual UAV, i.e., DJI PHANTOM 3 SERIES. For the safety of the experiment, the maximum charging current is adjusted to 3 A. As shown in Fig. 19(a), during the complete charging process, the 3 A constant charging current and 17.4 V constant charging voltage are achieved. The maximum power test result is shown in Fig. 19(b), the charging power of the system is 52.2 W, and the whole system efficiency is 84.8%. It is obvious that the developed wireless charging system is available for the UAV automatic charging. The power

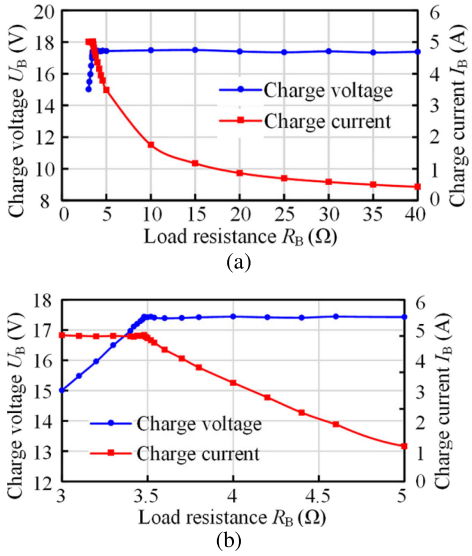

Fig. 16. Charging voltage and charging current versus load resistance. (a) Change the load resistance from 3 to 40 Ω. (b) Change the load resistance from 3 to 5 Ω.

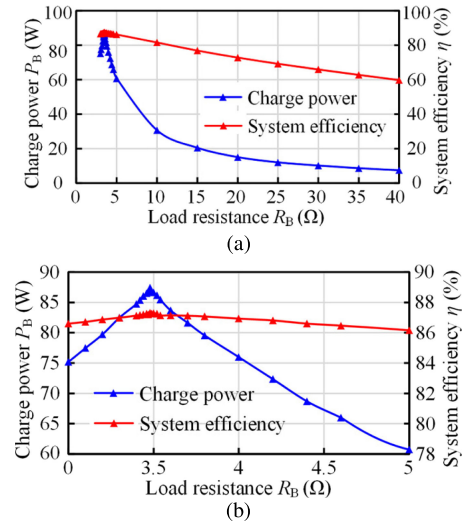

Fig. 17. Charging power and charging efficiency versus load resistance. (a) Change the load resistance from 3 to 40 Ω. (b) Change the load resistance from 3 to 5 Ω.

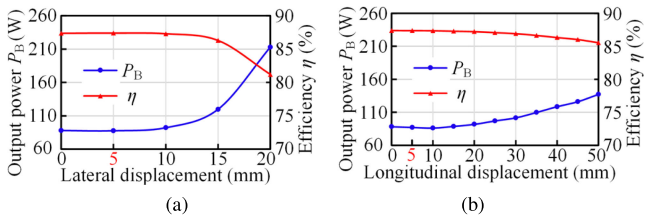

Fig. 18. Charging power and system efficiency versus (a) lateral displacement and (b) longitudinal displacement.

level of the system designed in this article is small, so only one transmitter and one receiver can meet the requirements. As for weight balance, the charging circuit can be shifted to the other side of the UAV. It should be mentioned that the proposed scheme is also suitable for high-power applications. Sometimes

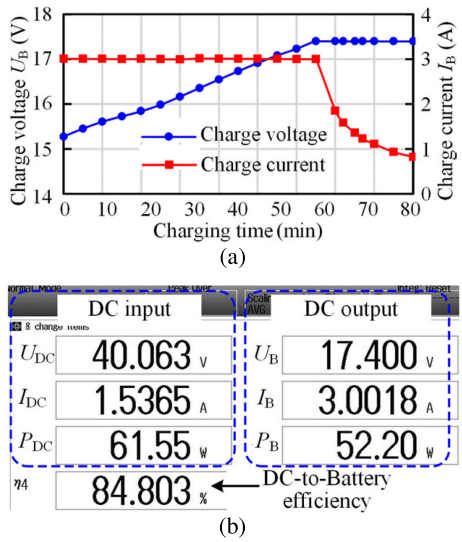

Fig. 19. (a) Charging voltage and charging current versus charging time. (b) Maximum power point test.

two parallel subsystems are required to improve the power level, optimize heat dissipation and balance the weight distribution of the UAV, which means two transmitters and two receivers (two receivers mounted on two landing gears respectively) are required. Because the proposed magnetic coupler has the characteristics of small volume and small operation space of magnetic field, it can be considered that there is no coupling between the two subsystems, which ensures good scalability of the proposed design.

VI. Conclusion

This article has focused on the development of a light weight and low-leakage magnetic interference UAV wireless charging system, which is applicable to an unattended charging of the UAV. And, to that end, an optimized orthogonal magnetic structure, a primary controlled wireless charging scheme, and a wireless charging station with position correction aid device are developed. The proposed magnetic coupler is able to reduce the weight and leakage magnetic flux emission, and enhance the coupling ability. The designed wireless charging circuit based on primary-side power control can further reduce the weight of a UAV's on-board circuit. The developed position correction aid scheme can achieve high-precision alignment with a simple structure and low cost, which ensures that the UAV is charged reliably and efficiently every time. The simulation and experimental results prove that the proposal is expected to be further applicable to the UAV unattended charging in the further.

References

[1] T. He, Y. Zeng, and Z. Hu, "Research of multi-rotor UAVs detailed autonomous inspection technology of transmission lines based on route planning," *IEEE Access*, vol. 7, pp. 114955–114965, 2019.

[2] S. Sawadsitang, D. Niyato, P. Tan, and P. Wang, "Joint ground and aerial package delivery services: A stochastic optimization approach," *IEEE Trans. Intell. Transp. Syst.*, vol. 20, no. 6, pp. 2241–2254, Jun. 2019.

[3] N. Kumar, D. Puthal, T. Theocharides, and S. P. Mohanty, "Unmanned aerial vehicles in consumer applications: New applications in current and future smart environments," *IEEE Consum. Electron. Mag.*, vol. 8, no. 3, pp. 66–67, May 2019.

[4] J. M. Arteaga, S. Aldhaher, G. Kkelis, C. Kwan, D. C. Yates, and P. D. Mitcheson, "Dynamic capabilities of Multi-mhz inductive power transfer systems demonstrated with batteryless drones," *IEEE Trans. Power Electron.*, vol. 34, no. 6, pp. 5093–5104, Jun. 2019.

[5] S. Aldhaher, P. D. Mitcheson, J. M. Arteaga, G. Kkelis, and D. C. Yates, "Light-weight wireless power transfer for mid-air charging of drones," in *Proc. 11th Eur. Conf. Antennas Propag.*, 2017, pp. 336–340.

[6] Y. Song, X. Sun, H. Wang, W. Dong, and Y. Ji, "Design of charging coil for unmanned aerial vehicle-enabled wireless power transfer," in *Proc. 8th Int. Conf. Power Energy Syst.*, 2018, pp. 268–272.

[7] J. Zhou, B. Zhang, W. Xiao, D. Qiu, and Y. Chen, "Nonlinear parity-time-symmetric model for constant efficiency wireless power transfer: Application to a drone-in-flight wireless charging platform," *IEEE Trans. Ind. Electron.*, vol. 66, no. 5, pp. 4097–4107, May 2019.

[8] T. Campi, F. Dionisi, S. Cruciani, V. De Santis, M. Feliziani, and F. Maradei, "Magnetic field levels in drones equipped with wireless power transfer technology," in *Proc. Asia-Pacific Int. Symp. Electromagn. Compat.*, 2016, pp. 544–547.

[9] T. Campi, S. Cruciani, F. Maradei, and M. Feliziani, "Wireless charging system integrated in a small unmanned aerial vehicle (UAV) with high tolerance to planar coil misalignment," in *Proc. Joint Int. Symp. Electromagn. Compat.*, Sapporo, Japan, 2019, pp. 601–604.

[10] D. Ke, C. Liu, C. Jiang, and F. Zhao, "Design of an effective wireless air charging system for electric unmanned aerial vehicles," in *Proc. 43rd Annu. Conf. IEEE Ind. Electron. Soc.*, 2017, pp. 6949–6954.

[11] B. Park *et al.*, "Wireless charging system using soft magnetic composite for unmanned aerial vehicle," *Int. J. Commun.*, vol. 2, no. 1, pp. 59–62, 2017.

[12] K. Song, P. Zhang, Z. Chen, G. Yang, J. Jiang, and C. Zhu, "A high-efficiency wireless power transfer system for unmanned aerial vehicle considering carbon fiber body," in *Proc. 22nd Eur. Conf. Power Electron. Appl.*, 2020, pp. 1–7.

[13] Z. Zhang, H. Pang, A. Georgiadis, and C. Cecati, "Wireless power transfer—An overview," *IEEE Trans. Ind. Electron.*, vol. 66, no. 2, pp. 1044–1058, Feb. 2019.

[14] T. Campi, S. Cruciani, M. Feliziani, and F. Maradei, "High efficiency and lightweight wireless charging system for drone batteries," in *Proc. AEIT Int. Annu. Conf.*, 2017, pp. 1–6.

[15] C. Song *et al.*, "EMI reduction methods in wireless power transfer system for drone electrical charger using tightly coupled three-phase resonant magnetic field," *IEEE Trans. Ind. Electron.*, vol. 65, no. 9, pp. 6839–6849, Sep. 2018.

[16] C. Cai, S. Wu, M. Qin, and Z. Yang, "A novel magnetic coupler for unmanned aerial vehicle wireless charging systems," in *Proc. IEEE Int. Power Electron. Appl. Conf. Expo.*, 2018, pp. 1–5.

[17] C. Cai, S. Wu, L. Jiang, Z. Zhang, and S. Yang, "A 500-W wireless charging system with lightweight pick-up for unmanned aerial vehicles," *IEEE Trans. Power Electron.*, vol. 35, no. 8, pp. 7721–7724, Aug. 2020.

[18] W. Han, K. T. Chau, C. Jiang, W. Liu, and W. H. Lam, "Design and analysis of quasi-omnidirectional dynamic wireless power transfer for fly-and-charge," *IEEE Trans. Magn.*, vol. 55, no. 7, pp. 1–9, Jul. 2019, Art. no. 8001709.

[19] T. Campi, S. Cruciani, G. Rodríguez, and M. Feliziani, "Coil design of a wireless power transfer charging system for a drone," in *Proc. IEEE Conf. Electromagn. Field Comput.*, 2016, p. 1.

[20] C. Cai, J. Wang, H. Nie, P. Zhang, Z. Lin, and Y. -G. Zhou, "Effective-configuration WPT systems for drones charging area extension featuring quasi-uniform magnetic coupling," *IEEE Trans. Transp. Electrific.*, vol. 6, no. 3, pp. 920–934, Sep. 2020.

[21] J. Li, F. Yin, L. Wang, B. Cui, and D. Yang, "Electromagnetic induction position sensor applied to anti-misalignment wireless charging for UAVs," *IEEE Sensors J.*, vol. 20, no. 1, pp. 515–524, Jan. 2020.

[22] B. Zhang, Q. Chen, G. Ke, L. Xu, X. Ren, and Z. Zhang, "Coil positioning based on DC pre-excitation and magnetic sensing for wireless EV charging," *IEEE Trans. Ind. Electron.*, to be published, doi: 10.1109/TIE.2020.2984435.

[23] Z. Li, S. Dong, K. Song, C. Zhu, Q. Zhang, and X. Huang, "Adaptive position alignment for wireless charging system with mutual inductance estimation and P&O algorithms employ only primary-side electrical parameters," *IET Power Electron.*, vol. 12, no. 10, pp. 2493–2500, 2019.

[24] C. H. Choi, H. J. Jang, S. G. Lim, H. C. Lim, S. H. Cho, and I. Gaponov, "Automatic wireless drone charging station creating essential environment for continuous drone operation," in *Proc. Int. Conf. Control, Autom. Inf. Sci.*, 2016, pp. 132–136.
[25] J. Schneider and J. O'Hare, "Alignment, verification, and optimization of high power wireless power charging systems," U.S. Patent 9 637 014B2, May 2017.
[26] W. Ni *et al.*, "Radio alignment for inductive charging of electric vehicles," *IEEE Trans. Ind. Inf.*, vol. 11, no. 2, pp. 427–440, Apr. 2015.
[27] A. Rohan, M. Rabah, M. Talha, and S. H. Kim, "Development of intelligent drone battery charging system based on wireless power transmission using hill climbing algorithm," *Appl. System Innov.*, vol. 44, no. 1, pp. 1–19, 2018.
[28] N. Khan, H. Matsumoto, and O. Trescases, "Wireless electric vehicle charger with electromagnetic coil-based position correction using impedance and resonant frequency detection," *IEEE Trans. Power Electron.*, vol. 35, no. 8, pp. 7873–7883, Aug. 2020.
[29] M. R. Barzegaran, H. Zargarzadeh, and O. A. Mohammed, "Wireless power transfer for electric vehicle using an adaptive robot," *IEEE Trans. Magn.*, vol. 53, no. 6, pp. 1–4, Jun. 2017, Art. no. 7205404.
[30] J. Huh, S. W. Lee, W. Y. Lee, G. H. Cho, and C. T. Rim, "Narrow-width inductive power transfer system for online electrical vehicles," *IEEE Trans. Power Electron.*, vol. 26, no. 12, pp. 3666–3679, Dec. 2011.
[31] Y. H. Sohn, B. H. Choi, E. S. Lee, G. C. Lim, G. Cho, and C. T. Rim, "General unified analyses of two-capacitor inductive power transfer systems: Equivalence of current-source SS and SP compensations," *IEEE Trans. Power Electron.*, vol. 30, no. 11, pp. 6030–6045, Nov. 2015.
[32] M. J. Neath, A. K. Swain, U. K. Madawala, and D. J. Thrimawithana, "An optimal PID controller for a bidirectional inductive power transfer system using multiobjective genetic algorithm," *IEEE Trans. Power Electron.*, vol. 29, no. 3, pp. 1523–1531, Mar. 2014.
[33] S. Zhou and C. Chris Mi, "Multi-paralleled LCC reactive power compensation networks and their tuning method for electric vehicle dynamic wireless charging," *IEEE Trans. Ind. Electron.*, vol. 63, no. 10, pp. 6546–6556, Oct. 2016.
[34] K. Song, Z. Li, J. Jiang, and C. Zhu, "Constant current/voltage charging operation for series–series and series–parallel compensated wireless power transfer systems employing primary-side controller," *IEEE Trans. Power Electron.*, vol. 33, no. 9, pp. 8065–8080, Sep. 2018.

Shuai Wu received the B.S. degree in electrical engineering and automation from Shanxi Agricultural University, Jinzhong, China, in 2017, and the M.S. degree in electrical engineering in 2019 from the Harbin Institute of Technology, Weihai, China, where he is currently working toward the Ph.D. degree.

His current research interests include wireless power transfer for autonomous underwater vehicles and unmanned aerial vehicles.

Chunwei Cai (Member, IEEE) was born in Shandong, China, in 1977. He received the B.S. and M.S. degrees in control theory and control engineering from Shan Dong University, Jinan, China, in 2001 and 2004, respectively, and the Ph.D. degree in electrical engineering from the Harbin Institute of Technology (HIT), Harbin, China, in 2013.

Since 2006, he has been working as a Lecturer at HIT, Weihai, China, where he has been working as an Assistant Professor since 2014. His current research interests include wireless power transfer systems, power converters, and inverters.

Longyun Jiang was born in Shandong, China, in 1997. He received the B.S. degree in electrical engineering and automation from Qingdao University of Technology, Qingdao, China, in 2019. He is currently working toward the M.S. degree in electrical engineering with the Academy of New Energy, Harbin Institute of Technology, Weihai, China.

His current research interests include power electronics and wireless power transfer system for unmanned aerial vehicle.

Jiawen Li was born in Sichuan, China, in 1998. He received the B.S. degree in electrical engineering and automation from the Harbin Institute of Technology, Weihai, China, in 2020. He is currently working toward the M.S. degree in control science and control engineering with the Academy of Automation, Southeast University, Nanjing, China.

His current research interests include pattern recognition and intelligent system for robot.

Shiyan Yang received the B.S. and M.S. degrees in electrical engineering and the Ph.D. degree in welding engineering from the Harbin Institute of Technology, Harbin, China, in 1984, 1989, and 1998, respectively.

He is currently a Professor with the Department of Electrical Engineering, Harbin Institute of Technology. His research interests include high-power power supply and its application, energy storage system and its equilibrium, and fundamental theory of finite power supply drive and key commonsense problem.